Constraining Microwave Brightness Temperatures by Radar Brightband Observations

A. BATTAGLIA

Department of Physics, University of Ferrara, Ferrara, Italy

C. KUMMEROW

Department of Atmospheric Science, Colorado State University, Fort Collins, Colorado

DONG-BIN SHIN

School of Computational Sciences, George Mason University, Fairfax, Virginia

C. WILLIAMS

CIRES–NOAA/Aeronomy Laboratory, Boulder, Colorado

(Manuscript received 19 August 2002, in final form 15 October 2002)

ABSTRACT

Multichannel microwave sensors make it possible to construct physically based rainfall retrieval algorithms. In these schemes, errors arising from the inaccuracy of the physical modeling of the cloud system under observation have to be accounted for. The melting layer has recently been identified as a possible source of bias when stratiform events are considered. In fact, Tropical Rainfall Measuring Mission (TRMM) Microwave Imager (TMI) observations reveal systematic differences in the observed brightness temperatures between similar rain profiles that often differ only by the presence or absence of a bright band.

A sensitivity study of the scattering properties of the melting layer with different one-dimensional steady-state microphysical and electromagnetic models is performed. The electromagnetic modeling of the ice particle density and assumption of the ventilation coefficient parameterization is found to have the greatest impact on the extinction profiles. Data taken from a 0.915-GHz National Oceanic and Atmospheric Administration (NOAA) profiler during the Kwajalein Experiment (KWAJEX) field campaign are used to reduce the uncertainties in the modeling of the bright band. The profiler data reduce the number of viable parameterizations, which in turn leads to a reduction in the variability of the upwelling radiances (simulated at TMI angle) for different cloud simulations.

Using the parameterizations that best match the profiler data, the brightness temperatures T_B generally increase if mixed-phase precipitation is included in the model atmosphere. The effect is most pronounced for systems with low freezing levels, such as a midlatitude cold front simulation. For TMI footprints at 10.65 GHz, the increase in the T_B from the bright band generally increases with rain rate and changes by as much as ~15–20 K. At 19.35 GHz the maximum effect is found around 3–5 mm h^{-1} (~15 K), and at 37 GHz the maximum effect is around 1 mm h^{-1} (~10 K), while at 85.5 GHz the effect is always lower than 3 K.

Despite the reduction of uncertainties achieved by using 915-MHz profiler data, differences between parameterizations are still significant, especially for the higher TMI frequencies. A validation experiment is proposed to solve this issue and to further reduce the uncertainties in brightband modeling.

1. Introduction

In stratiform rainfall, radar echoes often show a region of increased reflectivity in the area where ice crystals are melting. It is known as the ''bright band'' and is caused when relatively large, low-density ice particles acquire dielectric properties that are more similar to those of water before they collapse into water droplets below the melting layer.

This melting layer has recently been identified as a possible source of bias in microwave rainfall retrievals in stratiform regions (Olson et al. 2001a,b; Bauer et al. 1999). The large number of partially melted particles just below the freezing level has been shown to lead to significant excess absorption at all microwave frequencies relative to the absorption of only liquid rain or only ice hydrometeors with the same mass flux. The mixed-phase particle-absorption enhancement reveals itself as a peak both in the scattering (the well-known brightband

Corresponding author address: Dr. A. Battaglia, Dept. of Physics, University of Ferrara, Via Paradiso, 12, 44100 Ferrara, Italy.
E-mail: batta@fe.infn.it

peak in radar reflectivity) and in the absorption profile. Even though the melting layer may be only 0.5–1 km thick, its emission can be comparable to or even greater than that of the remaining rain layers, especially in the presence of very low freezing levels. From the spaceborne sensors perspective, this phenomenon has an immediate impact upon the retrieval of effective radar reflectivities below the freezing level and on the upwelling radiances measured by radiometers through increased T_Bs over cold surfaces.

As space-based rainfall retrieval algorithms have gained in sophistication, so has the need to properly address the brightband issue. For example, the attenuation correction algorithm of the Tropical Rainfall Measuring Mission (TRMM) precipitation radar (PR) (Iguchi et al. 2000) uses a different particle size distribution (PSD) and mixed-phase composition inside the bright band to address this issue. Unfortunately, there are virtually no measurements of this PSD, so the actual values of this PSD correspond largely to an unverified assumption. In an effort to better model the bright band, Olson et al. (2001a) modified the cloud-resolving models (CRMs) used by one of the passive microwave algorithms in TRMM by introducing mixed-phase hydrometeor species in the melting regions of the model. The analysis of the impact of this modification on TRMM Microwave Imager (TMI) simulations reveals that the increase in T_B due to the extra optical thickness, although moderated by the large footprint of the satellite sensors, can be as much as 16 K at 10.7 GHz, 15 K at 19.4 GHz, 12 K at 37 GHz, and 9 K at 85.5 GHz.

Generalizing the Olson et al. (2001a) approach of implementing a melting layer in precalculated CRM, Bauer (2001) tried to validate these findings using a restricted database of collocated TMI and PR stratiform observations. Using rain classification products provided by TRMM, the PR data were used to divide the dataset into stratiform events with and without a bright band. The accumulated frequency distributions of T_Bs coming from these two classes were compared with the ones computed by using different CRMs with and without melting. At low frequencies the CRM simulations with melting particles indeed showed an increase in T_B that better matched the observed T_B in the dataset containing bright bands. However, the CRM simulations predicted an increase at 37 and 85 GHz, which was not in agreement with the observations. Moreover, the cumulative distributions of T_Bs from different CRMs were quite different and distinct from the observed ones, even with the inclusion of a melting layer.

Despite efforts by Bauer (2001) to restrict the TMI database by selecting similar profiles with and without a bright band, observations show that the profiles are quite dissimilar. It appears that the presence or absence of a bright band introduces significant changes in the correlated microphysical character of the cloud, which makes such straightforward analyses impractical. Therefore, although the inclusion of melting effects in the CRM seems to better fit the observed data, this kind of analysis cannot be conclusive about the real effect of a melting layer on precipitation estimates.

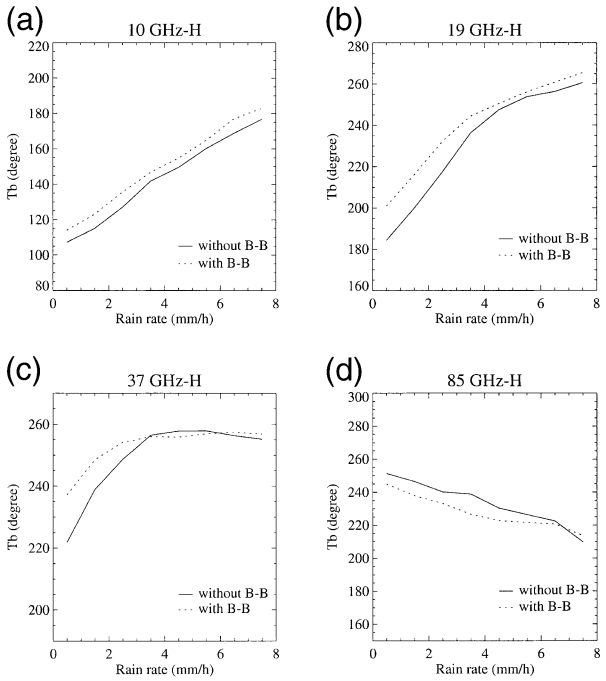

FIG. 1. Mean T_Bs (solid lines) and median T_Bs (dotted lines) as a function of the PR near-surface rain rates (2A25) for stratiform events with bright band and without bright band for four different TMI frequencies.

We performed an analysis of TRMM data for the 5-yr (1997–2001) December–January–February (DJF) period over the east Pacific; the TMI-T_B and PR-rain data collocated datasets have been analyzed for stratiform rain with and without a bright band. In addition, statistics were collated on the rainfall inhomogeneity to ensure that the presence or absence of a bright band did not affect the rainfall inhomogeneity, as this could also lead to a bias in the observed T_B. Inhomogeneity of rainfall, as determined from PR, was identical for rainfall with and without a bright band. Results for T_Bs (Fig. 1) show that at low-frequency channels (i.e., 10 and 19 GHz) there is a constant excess of the radiances for the brightband cases; this suggests that the emission peak has a relevant role. At 19 and 37 GHz, this excess tends to decrease as rain rate increases, probably due to the saturation of the optical thickness and the greater importance of scattering. The increases in the T_Bs typically range between 0 and 15 K, with the highest values found at low rainfall rates at 37 GHz. Finally, the decrease in the T_Bs at 85.5 GHz in the brightband cases seems to reveal that stratiform systems with a bright band have more ice and, thus, more scattering. These findings generally agree with Bauer (2001) and reveal that the bright band has an observable impact on the observations. It

therefore has to be accounted for in the modeling as well.

In this paper, we partially step back from these previous efforts in order to map the melting effect onto more basic radiative transfer quantities: the extinction profiles and the optical thickness. We begin by assessing the main uncertainties in the available parameterizations of the melting layer physics. This analysis has been performed by decoupling the problem from the CRM in order to estimate how the changes of these basic physical properties map onto measured quantities and how different CRMs affect this process.

In the past years, different models of the melting process have been developed (Yokoyama and Tanaka 1984; Klaassen 1988; Mitra et al. 1990; Fabry and Szyrmer 1999; Olson et al. 2001b). In order to address the various dynamical processes in nature, these models usually apply different parameterizations for the microphysical properties that drive the melting process (see Pruppacher and Klett 1997, chapter 16). Scattering properties at microwave frequencies are usually computed by treating melting particles as a uniform mixture of ice, water, and air with an effective dielectric constant. In this context, a variety of different methodologies have been developed that result in large variability in the electromagnetic properties of melting particles. All the different degrees of freedom in terms of microphysical and electromagnetic assumptions are briefly reviewed in section 2. The different parameterizations of the melting properties lead to a significant variability in the scattering properties relevant to the radiative transfer computation, as seen in section 3.

Constraints to the problem must come from experimental measurements. There are, unfortunately, no observations of k_{ext} profiles inside the bright band, but measurements of the optical depth of the melting layer can be inferred indirectly. An indirect inference was made by Olson et al. (2001b), who applied the mirror-image technique to the PR observations. The conclusions of this work qualitatively point to the fact that the presence of mixed-phase hydrometeors can at least partly explain the PR-observed optical depth distribution. The weakness of the approach lies in the fact that there are consistent uncertainties in the PR-retrieved optical thickness and that the melting model profiles were fully coupled to a CRM simulation, so that the complete natural variability observed by the PR may not have been captured.

Because of these difficulties we used the reflectivities and the Doppler velocities as measured from a 0.915-GHz profiler during the Kwajalein Experiment (KWAJEX) TRMM campaign. Although the profiler-derived quantities are only indirectly related to the physical quantities that drive the emission/absorption process, they help to reduce the uncertainties associated with the different microphysical and electromagnetic models. Section 4 summarizes procedures and results of profiler data–fitting analysis, together with a selection of the most appropriate models.

Section 5 uses the results of section 4, together with the new Goddard Cumulus Ensemble (GCE) CRM, to estimate the effect on brightness temperatures after the introduction of mixed-phase particles into the melting layer. Section 6 raises some ideas and questions on the melting layer effects to be addressed in future measurements and field campaigns. We underline which aspects, in our belief, represent the major uncertainties and deficiencies that arise from the modeling schemes. Finally, section 7 presents conclusions and final comments.

2. Review of existing models

A one-to-one correspondence between the ice particle falling across the freezing level and the raindrop into which it melts is generally accepted. This assumption implies that aggregation and breakup processes are negligible. While for breakup processes this seems to be occasionally true (Mitra et al. 1990) and occasionally not (Barthazy et al. 1998), aggregation processes, as pointed out by field observations (Barthazy et al. 1998; Heymsfield et al. 2002), seem to be present especially in the first half of the melting layer. Despite these considerations, it appears that the one-to-one correspondence is not a bad assumption in an average sense; Fabry and Zawadzki (1995) concluded that the combined effect of aggregation and breakup can account for less than a 1-dB change between the reflectivity just below and above the melting layer. In terms of the extinction properties, which are less sensitive to changes in the PSD than the reflectivity profiles, this effect should be even less important.

The new observations introduced in this study are from a 915-MHz profiler measuring reflectivities and Doppler velocities. To understand these observations, one must consider both a microphysical and an electromagnetic model. Microphysical properties refer to those properties that affect the evolution of the melting particle, such as its velocity, density, and fraction of melted water. Electromagnetic properties are those properties that affect the dielectric properties of the melting particles and thus the response of these particles to electromagnetic radiation. Microphysical models are well covered in the literature (Szyrmer and Zawadzki 1999, and references therein) and are reviewed only very briefly here; remarks are made only when different parameterizations are used.

a. Microphysical models

The rate of melting of a snowflake falling through the freezing level is driven by the humidity and temperature profiles of the surrounding environment; the latent heat available for melting closes the heating budget between the heat transferred to the particle surface

by conduction and that released/removed by condensation/evaporation. In terms of the mass fraction of melted water f this balance can be written as follows (details can be found in Szyrmer and Zawadzki 1999):

$$\frac{df}{dz} = \frac{24}{\rho_w L_f}\left[\frac{F_m(D_m)C_m}{V_m(D_m)D_w^3(D_m, \rho_s)}\right] \times \{K_{\text{air}}[T - T_0] + L_{\text{ev}}D_{\text{vap}}[\rho^{\text{vap}} - \rho_0^{\text{vap}}]\}, \quad (1)$$

where $\rho_w = 1$ g cm^{-3}, $L_f = 335$ J g^{-1}, T_0 is the temperature at the particle surface (assumed to be 273.15 K), T is the temperature of the environment, D_m is the diameter of the melting snowflakes, and D_w is the diameter of the final raindrop. The capacitance of the melting particle C_m coincides with the radius for spherical particles but takes on a complicated expression if melting particles are considered to be oblate spheroids (Mitra et al. 1990).

The solution of Eq. (1) practically solves the problem of the microphysical characterization of the melting process. But, while the terms in the curly braces ({ }) are fixed once the temperature and humidity profiles are known, the term in the square brackets ([ ]) presents many uncertainties related to different parameterizations in the velocity of the melting snowflake V_m, in the ventilation coefficient F_m, and in the snow density ρ_s.

1) Parameterization for melting velocities

Following the experimental work by Mitra et al. (1990), it is possible to parameterize the fall velocities of melting snowflakes as a function of v_s, the velocity of the initial snow particle, and v_r, the velocity of the final raindrop, as

$$V_m = y(f)(v_r - v_s) + v_s. \quad (2)$$

According to Mitra et al., the function $y(f)$ is practically independent of the flake size (Mitra et al. 1990, their Fig. 2) for dendritic crystals. A reasonable parameterization of the function $y(f)$ is given by

$$y(f) = \frac{f + f^2}{9.2 - 3.6(f + f^2)}, \quad (3)$$

while a well-established relationship for raindrop velocity is given by Atlas et al. (1973):

$$v_r(D_w)\ [\text{m s}^{-1}] = [9.65 - 10.3\ \exp(-6D_w\ [\text{cm}])]\left(\frac{\rho_0}{\rho_{\text{air}}}\right)^{0.5}, \quad (4)$$

where ρ_0 is the density of air at 1000 mb.

The snow velocities are not easily parameterized because ice particles of the same mass can have different fall speeds due to variations in the particle shape and bulk density. As a consequence, there is a fair amount of variability in the parameterizations of snowflake velocity present in the literature. A power-law relationship of the form

$$v_s(D_s)\ [\text{m s}^{-1}] = 4.84(D_s\ [\text{m}])^{0.25}\left(\frac{\rho_0}{\rho_{\text{air}}}\right)^{0.5} \quad \text{snow}, \quad (5)$$

$$v_g(D_s)\ [\text{m s}^{-1}] = 19.3(D_g\ [\text{m}])^{0.37}\left(\frac{\rho_0}{\rho_{\text{air}}}\right)^{0.5} \quad \text{graupel}, \quad (6)$$

is assumed for snow and graupel, respectively, and these relationships have been used hereafter. These relationships are consistent with the CRM simulations used later. Furthermore, because v_s is significantly smaller than v_r, the overall result is not particularly sensitive to a reasonable range of v_s.

2) Parameterization of the ventilation coefficient

The ventilation coefficient F in Eq. (1) depends on particle size and on the physical characteristics of the particle. This is an important factor in the microphysics of melting since all the variations in the fractional water mass are proportional to this quantity. Unfortunately, there are no direct studies of the ventilation coefficient of melting particles. Parameterization for the ventilation coefficient for raindrops/graupel/hail and snowflakes (Pruppacher and Klett 1997) are instead given as a function of the Schmidt number $\text{Sc} = \mu_{\text{air}}/\rho_{\text{air}}D_{\text{vap}} \approx 0.6$ and of the Reynolds number $\text{Re} = v_m L_m \rho_{air}/\mu_{\text{air}}$ [L_m is a length parameter, which for spherical particles coincides with the diameter, while for oblate spheroids it has been computed following Mitra et al. (1990)]:

$$F_m = a + b[\text{Sc}^{1/3}\ \text{Re}^{1/2}]^c \equiv a + b\chi^c, \quad (7)$$

where $a = 1$, $b = 0.14$, and $c = 2$ for $\chi \leq 1$, while $a = 0.86$, $b = 0.28$, and $c = 1$ for $\chi > 1$. Hereafter, according to the shape selected for melting particles, we will refer to Eq. (7) as the ''Mitra/sphere'' or ''Mitra/spheroid'' parameterization of the ventilation coefficient.

Another expression for F_m (hereafter the ''Szyrmer'' parameterization) is found in Szyrmer and Zawadzki (1999):

$$F_m = B_m\frac{(D_w\ [\text{cm}])^{A_m}}{D_m\ [\text{cm}]}, \qquad B_m = 33.0\ \text{cm}^{-0.7}, \qquad A_m = 1.7. \quad (8)$$

If Eq. (8) is used in Eq. (1), the dependence on melting particle diameter tends to cancel out (because of the product $F_m C_m$), so that, for a prescribed melted diameter D_w, the distance to melting is almost (except for a weak dependence in V_m) snow-density independent.

3) Parameterization for snow density

An important input to the model is the density of the snow above the bright band. It is well known that the

TABLE 1. Coefficients entering Eq. (9) for different parameterizations.

No. of density model	x_s	y_s	Reference
1	0.022	1.5	Magono and Nakamura (1965)
2	0.064	0.65	Schaller et al. (1982)
3	0.018	0.8	Barthazy et al. (1998)
4	0.015	1.18	Locatelli and Hobbs (1974)
5	0.012	1.0	Mitchell et al. (1990)
6	0.015	0.6	UW-NMS* model
7	0.1	0.0	GCE Model
8	0.4	0.0	Graupel

* University of Wisconsin-Nonhydrostatic Modeling System.

density of snow particles decreases markedly with size. Different relationships can be found in the literature. Table 1 lists some of the common ones; all of them are in cgs units and in the form

$$\rho_s(D_s) = \frac{x_s}{D_s^{y_s}}. \tag{9}$$

An upper limit equal to 0.92 g cm^{-3} has been fixed to avoid unrealistic densities. The density of graupel has been fixed at 0.4 g cm^{-3}.

The effect of the different microphysical parameterizations is shown in Fig. 2a. The velocities of a melting particle (having an equivalent raindrop diameter equal to 1 mm) are shown as a function of the altitude below the freezing level. To assess the importance of the parameterizations for F_m [Mitra (sphere/spheroid) + Szryrmer], different densities and velocities of the initial snowflakes are considered. Note that, in this analysis, we disregard Eq. (5), which would dictate a unique initial snow velocity once the final diameter and the initial density are prescribed.

The snowflake density and the ventilation coefficient seem to be the driving factors in the melting process. Generally, with Mitra parameterizations, denser snowflakes require more time to melt compared to fluffy ones, for both spheres and oblate spheroids. On the contrary, the Szyrmer parameterization leads to results that are density independent; in general, the distance required for complete melting is usually a little bit shorter than that for snowflakes with density equal to 0.1 g cm^{-3} in the Mitra/sphere parameterization. In contrast to density and ventilation parameterization, the initial snowflake velocity has much less influence on the distance to complete melting. The same conclusions can be drawn from Fig. 2b, in which the water mass fraction of melting particles is plotted as a function of the distance below the freezing level. For this example, the lapse rate was set to 6 K km^{-1} and a completely saturated humidity profile was chosen. Variations of the background conditions significantly modify the melting process and affect the brightband amplitude.

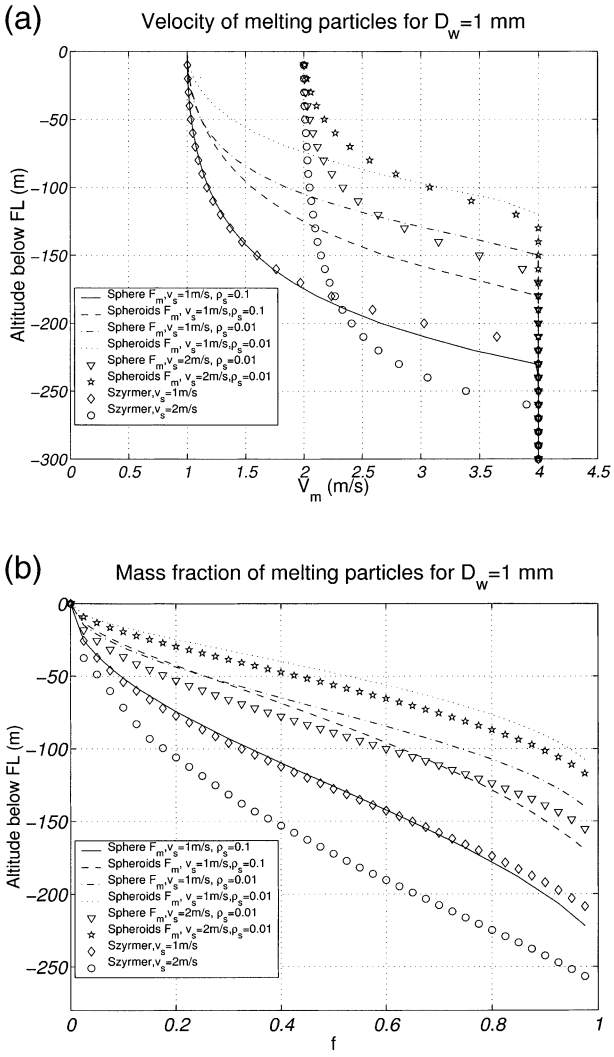

FIG. 2. (a) Velocities of melting particles as a function of the distance below the freezing level for ice particles that melts into a 1-mm-diameter raindrop for different ventilation coefficients, ice densities, and initial velocities. (b) Same as (a) but for the fraction of melted water.

b. *Electromagnetic models*

The exact solution of scattering and absorption of microwave radiation by melting particles (a mixture of air, water, and ice) is not practically feasible because of the lack of information concerning the detailed structure (shape, size, position, orientation, and number) of inhomogeneities present in the melting particles. Therefore, the only way to approach the problem is to determine some average optical properties of these heterogeneous materials and then to treat them like homogeneous substances described by an effective dielectric constant ϵ^{eff}, with a density equal to

$$\rho_m = \frac{m_s + m_w}{\dfrac{m_s}{\rho_s} + \dfrac{m_w}{\rho_w}} = \frac{\rho_s \rho_w}{[f\rho_s + (1 - f)\rho_w]}. \tag{10}$$

1) MAXWELL–GARNETT MODELS

In mixed-phase hydrometeor electromagnetic modeling (e.g., Fabry and Szyrmer 1999; Olson et al. 2001b) the most commonly used formula for the effective dielectric constant is that of Maxwell and Garnett. Among all 12 different combinations for accommodating air, water, and ice as matrices or inclusions, we consider only the ones most likely to reproduce experimental observations, as found in previous studies.

- Model MG_{wi}: The melting particle is described by a water matrix with dry snow inclusions. The snow, in turn, consists of an ice matrix with air inclusions:

$$\epsilon_{wi}^{eff} = \epsilon_{water//dry\text{-}snow} = \epsilon_{water//air\ inclusions\ in\ an\ ice\ matrix}. \quad (11)$$

- Model MG_{iw}: The melting particle is described by a dry snow matrix with water inclusions:

$$\epsilon_{iw}^{eff} = \epsilon_{dry\text{-}snow//water} = \epsilon_{air\ inclusions\ in\ an\ ice\ matrix//water}. \quad (12)$$

- Model MG1: The melting particle is described by a water matrix with dry snow (composed of ice inclusions in an air matrix) inclusions:

$$\epsilon_1^{eff} = e_{water//ice\ inclusions\ in\ an\ air\ matrix}^{eff}. \quad (13)$$

- Model MG2: The melting particle is described by a wet snow matrix (composed of ice inclusions in a water matrix) with air inclusions:

$$\epsilon_2^{eff} = \epsilon_{ice\ inclusions\ in\ a\ water\ matrix//air}. \quad (14)$$

- Model MG3: The melting particle is described by an air matrix with inclusions composed of a water matrix with ice inclusions:

$$\epsilon_2^{eff} = \epsilon_{air//ice\ inclusions\ in\ a\ water\ matrix}. \quad (15)$$

2) MENEGHINI AND LIAO MODELS

Instead of using the Maxwell–Garnett approach, Meneghini and Liao (1996) derived ϵ^{eff} using a numerical approach (the conjugate gradient method) to compute the electromagnetic mean internal fields, using a spatially uniform distribution of the components. The calculations are carried out only for ice–water mixtures. There are two possible parameterizations of their results.

- Model ML96 (Meneghini and Liao 1996) is an intermediate model between model MG_{wi} and model MG_{iw}. Wet snow is considered as a dry snow matrix with water inclusion at the initial phase of melting and as a water matrix with dry snow inclusions at the end of the melting process, with a continuous transition between the two states.
- Model ML00 (Meneghini and Liao 2000) provides a parameterization of the effective dielectric constant of ice–water mixtures for frequencies between 10 and 95 GHz or, equivalently, of the mean field ratio $\langle E_{water}\rangle / \langle E_{ice}\rangle$. Details about the derivation of the refractive index of melting particles can be found in Olson et al. (2001b).

3) COATED SPHERE MODEL

The coated sphere model takes into account that snowflake densities not only decrease with size but also vary continuously throughout the bulk of the same snowflake. To address this issue Fabry and Szyrmer (1999) modeled snowflakes as consisting of two concentric spheres (a core and a shell) with different densities, the outer shell representing a tenuous collection of collected ice crystals. Detailed formulas for computing the density of the inner core and of the outer shell and the relative position of the inner core at every stage of the melting process can be found in their paper. In order to describe the different distribution of the melted water inside the melting particles, two additional models were therefore implemented:

- model FS1: coated sphere with both core and shell as in MG3,
- model FS2: coated sphere with core as in MG2 and shell as in MG3.

Figure 3 shows the behavior of $\mathrm{Im}(K)$ and $|K|^2$ [$K = (\epsilon^{eff} - 1)/(\epsilon^{eff} + 2)$] at 10.65 GHz (the other frequencies show the same behavior). These factors completely determine the behavior of the extinction and of the scattering/backscattering coefficient in Rayleigh approximations. Figure 3 reveals the extreme behavior of model MG1 (practically equivalent to model MG_{wi}) and of model MG2 regarding both backscattering and extinction cross sections; these quantities, for particular values of the melted mass fraction, can be almost an order of magnitude greater than those coming from the other models. Similarly, the same figure shows significant differences between models MG3, ML96, and ML00. As a consequence of these findings, we can predict that, at the profiler frequency (well inside Rayleigh region), MG1 and MG2 will give the strongest bright-band peak, followed by MG3, ML96 (practically equivalent to model MG_{iw}), and ML00. The same considerations apply to the extinction peak, which is related to $\mathrm{Im}(K)$.

3. Uncertainties and analysis of profiler data

The most important effect of the bright band on rainfall retrieval algorithms (both radar and radiometers) is the excess extinction produced by melting particles. As already observed by Bauer et al. (1999), scattering properties such as the albedo and the asymmetry factor are of much less importance. A sensitivity analysis can thus be reduced to studying the effect of various parameterizations upon a single variable—the excess optical thickness, $\Delta\tau$. Sensitivity analyses are straightforward. They show that the uncertainty is dominated by the

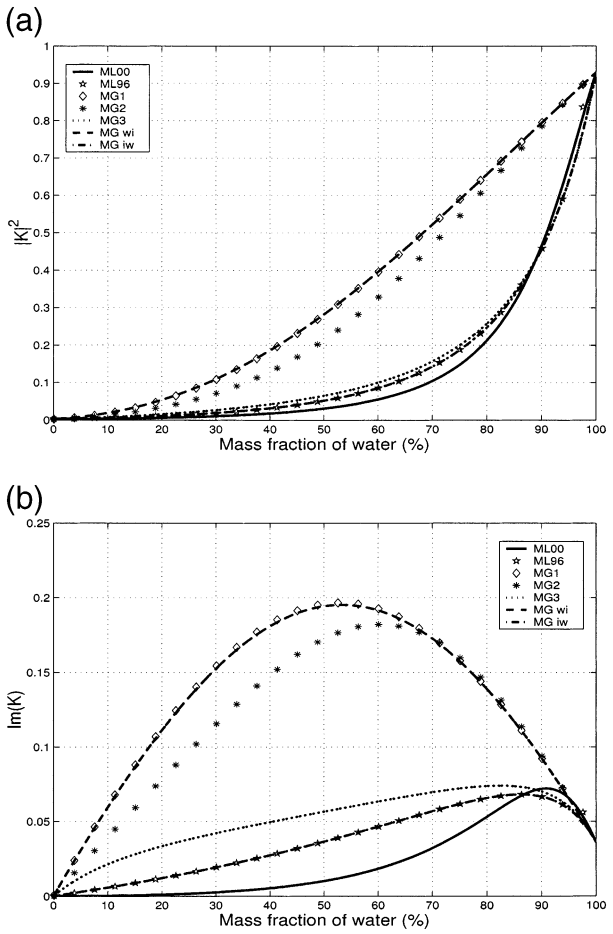

FIG. 3. The $|K|^2$ and Im(K) factors based upon different dielectric models at 10.65 GHz for an ice particle with density equal to 0.1 g cm^{-3}.

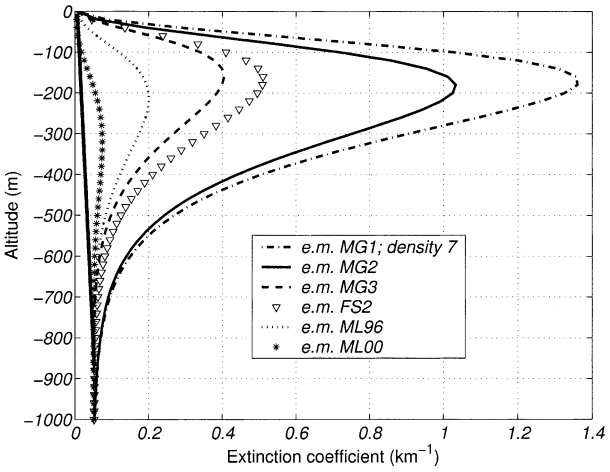

FIG. 4. Extinction profile at 10.35 GHz for a rainfall rate equal to 10 mm h^{-1}.

electromagnetic models; shown in Fig. 4 are extinction profiles for different electromagnetic models at 10 GHz for a Marshall and Palmer RR = 10 mm h^{-1}. The excess optical thickness with respect to no-mixed-phase models corresponds to the area subtended between each curve and the black continuous line. Clearly, different electromagnetic models have different impacts upon the extinction profile. This effect is most pronounced at low frequencies (e.g., 10 and 19 GHz). By comparing different electromagnetic models, we can conclude that ML00 produces the smallest increase in $\Delta\tau$, while MG1 and MG2 produce increases that can be an order of magnitude greater. ML96 gives excesses that are larger than those given by ML00 but still consistently lower than those of FS2 and MG3. FS1 and MG3 give almost the same answer. At higher frequencies (not shown), the backscattering peak disappears, but the extinction peak remains visible, although less pronounced. At frequencies such as 85 GHz, the increase in $\Delta\tau$ for ML and FS models gives extinction profiles as different as at low frequencies; at 85.5 GHz for example, ML models are quite similar to FS models.

The ventilation coefficient F_m, the snow density, and the background conditions determine how long particles remain in a ''melting'' state. This represents a secondary source of uncertainty. The Szyrmer parameterization of ventilation coefficient generally provides an upper estimate of $\Delta\tau$, and the Mitra/spheroid parameterization a lower boundary. Similarly, drier background conditions with lower lapse rates result in bigger $\Delta\tau$s. Very high density particles usually give lower $\Delta\tau$s at 10 and 19 GHz. This is particularly true for the models that have greater absolute excess $\Delta\tau$ (like MG2). For models MG3 FS and ML, only graupel-like particles have significantly lower $\Delta\tau$. On the other hand, at the highest frequencies, the variability due to density increases and graupel-like particles can give a substantial contribution to the optical thickness excess.

In order to restrict these uncertainties, we have analyzed data taken from a 0.915-GHz National Oceanic and Atmospheric Administration (NOAA) profiler (Carter et al. 1995) at the Kwajalein Atoll in the Marshall Islands from July 1999 to August 2000. Only stratiform events are considered. The advantage of using the profiler data is that we can use the reflectivity, the Doppler velocity, and the observed spectral width to constrain the problem. In particular, these three quantities allow us to retrieve the drop size distribution (DSD) of rain in the form of a gamma size distribution (Williams 2002). Therefore, by providing a complete microphysical characterization of the precipitation below the bright band, the profiler seems well suited to reconstruct the melting layer structure upward from the completely melted stage.

The drawbacks of this methodology are that the measured quantities are only indirectly related to the extinction profile and that the frequency of the profiler is significantly lower than those used by current microwave radiometers. Nevertheless, if the profiler observations can be correctly reproduced by a physical model,

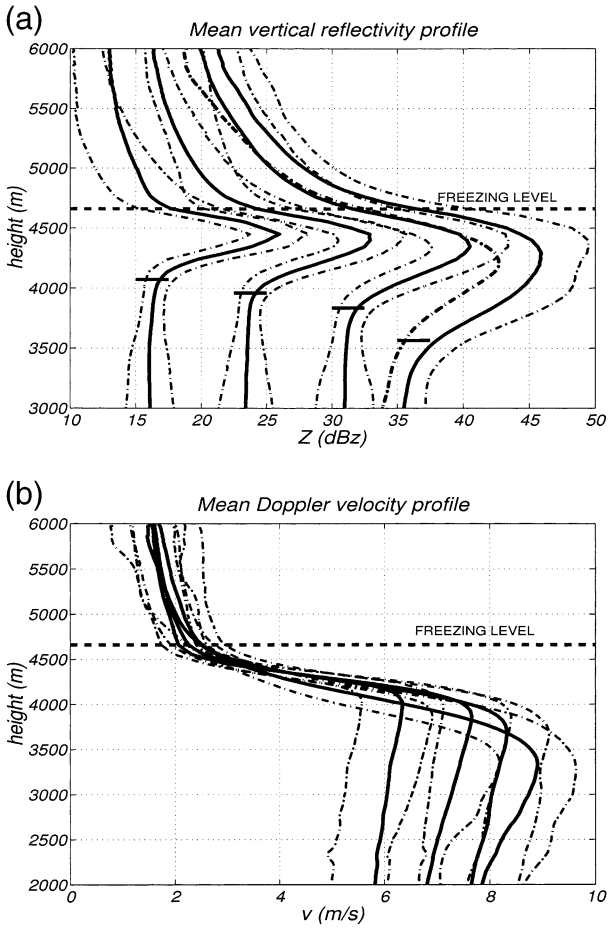

FIG. 5. Mean (continuous lines) and variance (dotted lines) for vertical reflectivity and Doppler velocity profiles.

then we can have confidence that both the microphysical process and the electromagnetic scattering of melting particles are reasonably reproduced. Therefore, the profiler data can be used to reduce the uncertainties in the brightband modeling.

In addition to DSD below the melting layer, the profiler data can be used to find the brightband top h_{FL} (coincident with the freezing level), and the brightband bottom h_{base}. These variables have been computed using both the reflectivity and the Doppler velocity profiles. From the reflectivity profile, variables are estimated by looking at the height where the curvature in the logarithm of the reflectivity profile is maximum [this technique has been proposed by Fabry and Zawadzki (1995)]; from the Doppler velocity profile variables are retrieved looking at the height at which the vertical gradient of the Doppler velocity becomes lower than 0.15 m s^{-1} (100 m^{-1}). In this study, we simply use the average of these two estimates.

Figure 5 shows the mean and the variance of the vertical reflectivity and Doppler velocity profiles in and around the bright band, as a function of the basal reflectivities Z_{rain} (defined as the mean reflectivity in a 200-m layer below h_{base}). The height of the bright band has been renormalized with respect to the estimated h_{FL}. The general signatures of the profiles follow the characteristics already identified by Fabry and Zawadzki (1995), although, in this case, the bright band is somewhat thicker. This can be attributed both to the partially different algorithm to estimate the boundaries of the melting layer and to a different climate regime for the region under investigation (a tropical oceanic island versus a midlatitude land site in Fabry and Zawadzki's study).

At the estimated h_{FL}, the Doppler velocity profiles are very narrowly distributed in the interval between 2 and 2.8 m s^{-1} (see Fig. 5, bottom). This is nearly impossible to achieve using one of the relationships described in Eq. (5). Therefore, the profiler data have been used to constrain v_s directly. Similarly, we found difficulties in fitting the mean Doppler widths at h_{FL}, where they spread out in the range 1.2–1.4 m s^{-1}. Unfortunately, the Doppler widths are strongly affected by the large variability in the fall speed–mass relationships for ice particles, by the random presence of vertical air motion, and by possible turbulence broadening, as noted by Passarelli and Srivastava (1980). The Doppler width is therefore not used in the brightband region. Only the reflectivity and velocity profiles are used to constrain the melting parameterizations.

Matching profiler data

Simulations carried out with different parameterizations show that the thickness of the melting layer and the position of the brightband peak are essentially driven by the density model, the ventilation coefficient, and the background conditions, while the intensity of the bright band is principally tuned by the electromagnetic and the density models. Since the background condition in the melting layer can vary significantly within and between precipitation events, the lapse rate is varied from 4 to 7 K km^{-1} in 1 K km^{-1} intervals. Two humidity profiles are used (one completely saturated and the other with a constant 10% km^{-1} decrease starting from saturated conditions at the freezing level). The temperature profiles are chosen to be in reasonable agreement with the variability of temperature structures below the freezing level as measured by the soundings performed at Kwajalien (the lapse rate of the period between July and September 1999 is 5.7 $\pm$ 0.8 K km^{-1}, while the freezing level was 4750 $\pm$ 210 m).

Since the estimation of the mean properties of the bright band is the primary focus of this study, profiles are binned in roughly 1–2-dBZ intervals according to the reflectivity just below the bright band. For each profile, the drop size distribution is retrieved from the profiler data at this location h_{base}. It is represented by $n_w(D_w)$. Then the PSD is allowed to evolve by preserving the mass flux, so that a generic PSD of melting

TABLE 2. Best combined electromagnetic and density model for the three parameterizations used. Different categories with basal reflectivities in different ranges are considered. The distance, summed up over 100 profiles, is shown in parentheses.

Z_{rain} range dBZ	No. of profiles	Parameterization for F_m		
		Mitra/sphere	Mitra/spheroid	Szyrmer
17.5–20	462	FS2//7 (1.75)	FS2//2 (1.87)	MG3//5 (1.67)
20–22	570	FS2//7 (1.73)	FS2//2 (1.97)	MG3//5 (1.65)
22–24	580	FS2//7 (1.91)	FS2//2 (2.12)	MG3//5 (1.77)
24–25	247	FS2//7 (1.97)	FS2//2 (2.06)	MG3//5 (1.82)
25–26	303	FS2//7 (1.94)	FS2//7 (2.29)	MG3//5 (1.75)
26–27.5	427	FS2//7 (2.07)	FS2//7 (2.34)	FS1//5 (1.84)
27.5–30	411	FS2//7 (2.23)	FS2//7 (2.37)	FS1//5 (1.97)
30–32	158	FS2//2 (2.3)	FS2//7 (2.43)	FS1//5 (2.04)
32–34	140	FS2//2 (2.3)	FS2//7 (2.28)	FS1//5 (1.98)

particles $n_m(D_w)$, expressed in terms of the melted diameter D_w, is given by

$$n_m(D_w)v_m(D_m) = n_w(D_w)v_w(D_w). \quad (16)$$

For each simulated PSD in the bright band, hydrometeor characteristics are simulated using the different background conditions, the eight density models, and the electromagnetic models. The simulated curves for each profile are then rescaled in order to match the onset of melting with h_{FL}, the estimated freezing level.

To give a measure of the proximity of two profiles, we define the distance between Doppler velocity profiles by

$$\text{dist}_{vel} = \frac{\left\{\sum_h [V_{true}(h) - V_{sim}(h)]^2\right\}^{1/2}}{\langle V_{true}\rangle}, \quad (17)$$

and between reflectivity profiles by

$$\text{dist}_{ref} = \frac{\left\{\sum_h [Z_{true}^{1/6}(h) - Z_{sim}^{1/6}(h)]^2\right\}^{1/2}}{\langle Z_{true}^{1/6}\rangle}, \quad (18)$$

where the sum extends to all the bins within the bright band. The best background condition is selected by minimizing the total distance for each profile dist = dist_{ref} + dist_{vel}.

For each basal reflectivity bin, the best-fitting density, ventilation coefficient, and electromagnetic model are summarized in Table 2. The range of values obtained from the different parameterizations is synthesized in Fig. 6. Among the different ventilation parameterizations, Table 2 indicates that the Szyrmer parameterization is the most appropriate. However, it is important to underline that this result is very sensitive to the selected background conditions.

Within the Szyrmer parameterization, MG3 and FS1 (which give almost identical results), in conjunction with density model 5, seem to give consistently the best results. FS2 (in conjunction with density models 1 and 2) is the next best electromagnetic model, and it seems to give better results for profiles that have higher than the mean reflectivity profile. The ML models generally underestimate the reflectivity peak, so that they are suitable for fitting only weak bright bands. On the other hand, MG1 and MG2 (green lines in Fig. 6) produce reflectivity peaks that are too high (in conjunction with snowlike densities) or too low (in conjunction with graupel-like densities) compared with observations.

One should note, however, that the above conclusions apply to mean observed profiles rather than any one specific observation. The simulated velocity profiles generally show a good agreement with profiler data except at the onset of melting, when the model Doppler velocities tend to increase more slowly than the observed ones. In addition, the lapse rate and the vertical velocity of air in the melting layer can vary significantly within and between precipitation events, and this variability has not been completely addressed since no background conditions were measured simultaneously with the profiler data. Finally, since the reflectivity profile is very sensitive to the PSD, the one-to-one particle correspondence between the freezing and the basal levels is certainly a source of bias also. As such, the better or worse fit of any one parameterization should not be viewed as a shortcoming of the parameterization itself.

For studies requiring mean brightband properties, however, the profiler data analysis allows us to rule out some of the microphysical and electromagnetic parameterizations, at least for tropical oceanic precipitation. In the microphysical context, the parameterization in Equation (8) seems to fit the experimental measurements quite well, with models MG3 and FS2 bracketing the mean reflectivity peak; models ML96 and ML00 seem to underestimate the peak in the average sense. We can thus conclude that models MG3 and FS2 should supply two boundary limits when computing the extinction coefficient. Graupel-like densities are much less compatible with the profiler measurements and, in any case, only if coupled with model MG2.

4. Impact on T_Bs and rainfall estimates

To understand the impact of melting particles on T_Bs, it is useful to begin with as realistic a cloud representation as possible. Two simulations from the GCE model

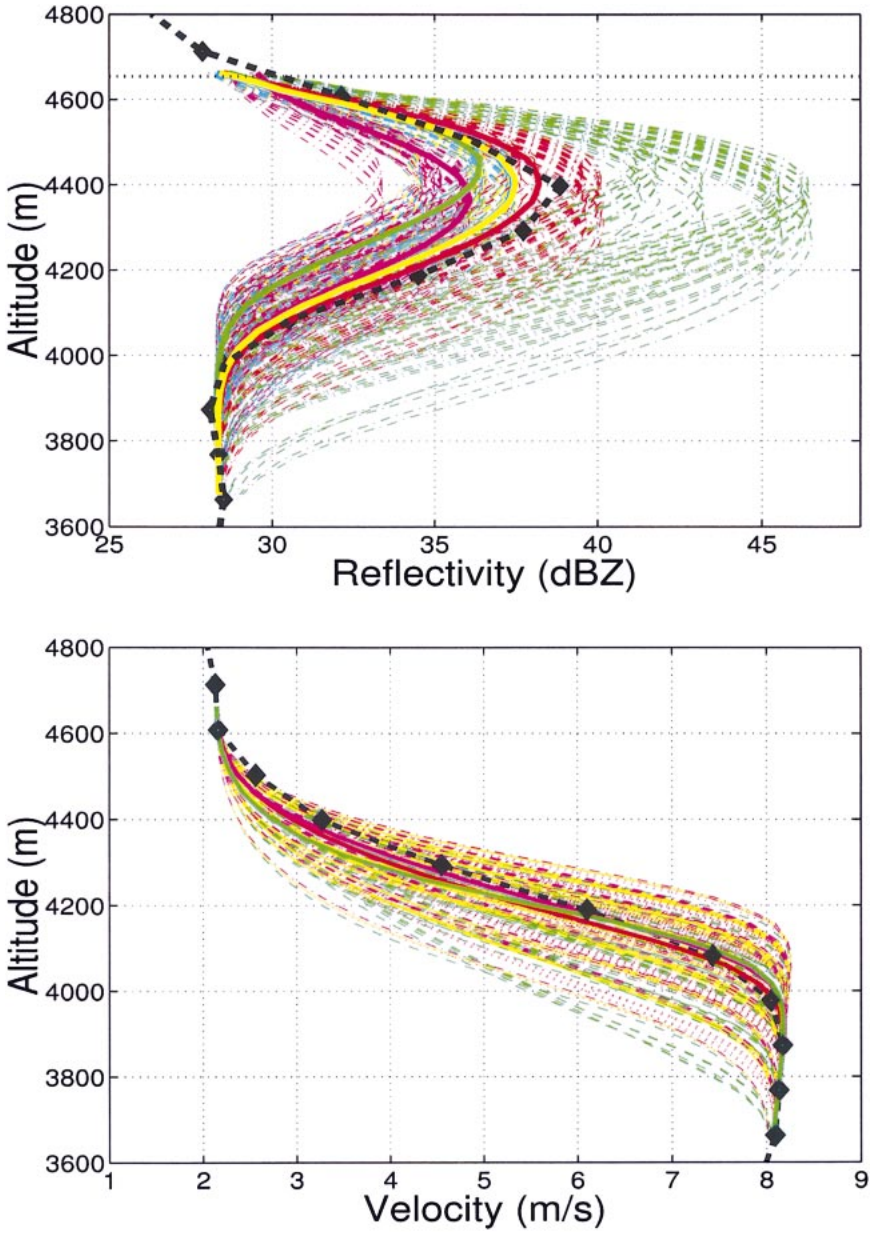

FIG. 6. Best-fitting curves, with varying background conditions and density assumptions to (top) a selected reflectivity and (bottom) velocity profile. Different colors correspond to different electromagnetic models (ML96 = magenta; MG2 = green; MG3 = yellow; FS1 = cyan; FS2 = red). The black diamonds are the profiler data. The thicker lines correspond to the best matching profiles selected for every different electromagnetic model.

(Tao and Simpson 1993) have been used for this purpose: a tropical oceanic squall line and a midlatitude oceanic cold front (Chiu and Petty 2001). The CRMs provide hydrometeor profiles, temperature, and humidity vertical structure (at a 500-m vertical resolution in the lower troposphere), but they do not include mixed-phase hydrometeors. The cold front is characterized by prefrontal shallow convection and well-developed rainbands aligned to the frontal line along the southwest–northeast direction, significant amounts of snow, and a low freezing level (FL = 2.7 ± 0.4 km), while the tropical squall line contains mostly graupel and has a much higher freezing level (FL = 5.0 ± 0.1 km).

For each simulation, the pixels classified as stratiform are altered by introducing a one-dimensional melting model. This modification follows the scheme already used in fitting the profiler data. The basal level h_{base} is estimated as the level where no ice-type hydrometeors are present; from this height, and using the CRM background conditions and rain DSD assumptions in the

model, the mixed-phase hydrometeor profile (at 25-m vertical resolution) is constructed up to the freezing level for the different microphysical models. A mass flux correction is carried out by adjusting the N_0 parameter of the PSD at each level so that the melting particle flux is equal to the parent model mass flux. Above the freezing level, all rain is converted to ice-type hydrometeors. Because the profiler data was inconsistent with high-density particles in a bright band, graupel particles in the tropical oceanic squall-line simulation were converted to mass-flux-equivalent snow content. This conversion is certainly heavy-handed but necessary to match our particular observations. In field measurements during the KWAJEX and Large Scale Biosphere–Atmosphere Experiment in Amazonia (LBA) TRMM field campaigns (Heymsfield et al. 2002), images from cloud particle imagers (CPIs) indicate very little graupel at the freezing level in stratiform clouds having well-defined bright bands. As such, the large amounts of graupel produced in the stratiform region by the tropical squall-line simulations seem inconsistent with a number of observations and may represent a problem with the microphysical schemes used in that model. Moreover, melting layer effects of graupel-like particles in squall line simulations have been already carefully treated in the literature (e.g., Olson et al. 2001a). In the cold front this feature is well reproduced by the model. Denser graupel falls out in close proximity to the convective updraft only, and small contents of graupel are present in the pixels classified as stratiform (and only for rain rates higher than 20 mm h^{-1}).

With these approximations, it is now possible to isolate the effect of the bright band upon upwelling radiances that would be measured by a satellite. For each profile, the scattering properties have been computed, with and without the brightband modifications. The most likely electromagnetic parameterizations (as found in section 3) have been used in the simple Mie theory context. In addition, the methodology has been repeated without the results of section 3 in order to illustrate the reduction in uncertainty coming from the profiler observations. Figure 7 shows the increase in T_Bs due to the brightband introduction at 10.65 GHz for the cold front case at the CRM resolution as a function of the CRM rain rate at the ground. The initial uncertainty stemming from the variety of electromagnetic models is reflected in a wide range of T_B variations for each rain rate. The profiler analysis, by bracketing the electromagnetic choice between MG3 and FS2 models, considerably reduces the variability as shown by the single lines.

a. The optical thickness excess $\Delta\tau$

As already discussed, the most important aspect of the bright band is the increase in the optical thickness. This excess is not very sensitive to individual CRM simulations. The variability in $\Delta\tau$ is almost entirely described by the variability in the melting and electromagnetic models, relying on the CRM only to supply mass flux variations inside the melting layer and variability in the temperature and humidity structures of each profile. The strength of the excess $\Delta\tau$ behaves as a forecast at the end of section 3 from the profiler analysis. Biases between different models increase with the basal reflectivities so that, from a validation point of view, it seems easier to discriminate between models at high rainfall rates. In terms of ΔT_Bs (see section 4c), it turns out that small changes in $\Delta\tau$ at low rainfall rates can also have significant impact on the T_Bs, so the entire range of basal reflectivities needs to be considered.

b. Effect of the optical thickness excess on T_Bs

In general, the impact of a brightband extinction excess upon upwelling T_B strongly depends on the strength of the weighting function in the proximity of the freezing level. To gain some insight into this behavior, a very simple pure absorptive model is built. This approximation may be representative at the 10.7-GHz TMI frequency. The atmosphere is described in terms of three isothermal layers: 1) the bright band (responsible for 15% and 25% of the total optical thickness for a tropical squall line and an extratropical cold front, respectively) at a temperature of $T_0 = 273.15$ K; 2) the underlying layers (responsible for 75% and 50%) at a mean atmospheric temperature $\langle T_{\rm atm}\rangle$ computed as the average of T_0 and the surface temperature (300 and 293 K for the squall line and the cold front, respectively); and 3) the upper layer above the bright band at 265 K. The response of T_Bs to an increase of optical thickness in the brightband layer can be predicted once the total optical thickness without melting layer and the relative excess due to melting hydrometeors are known. As already observed by Olson et al. (2001a), the increase in T_B is roughly equal to

$$\Delta T_B = \underbrace{(1 - e_s)\langle T_{\rm atm}\rangle \exp(-2\tau_{\text{no-melt}}/\cos\theta_v)}_{\text{factor I}} \underbrace{[1 - \exp(-2\Delta\tau/\cos\theta_v)]}_{\text{factor II}}. \quad (19)$$

The variations in T_B are modulated by two opposite factors: the difference between the average atmospheric temperature and the T_B without including the melting layer (factor I), and a factor related to the square of the

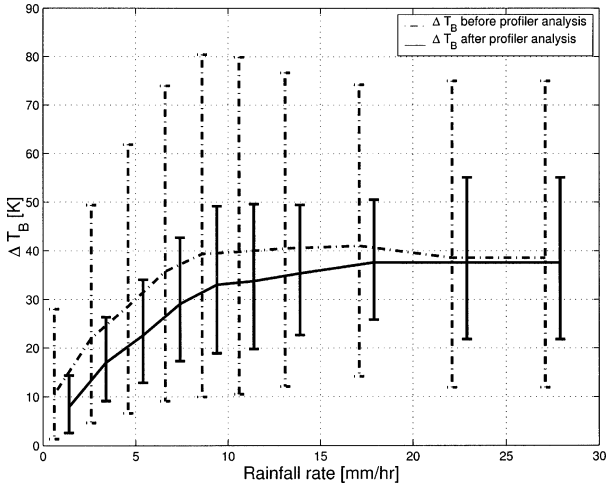

FIG. 7. Mean and std dev of the increase in T_Bs at 10.35 GHz for the cold front case at the CRM resolution as a function of the CRM rain rate at the ground. Note the reduction in the uncertainties in T_B after the profiler analysis.

transmissivity of the pure brightband excess (factor II). For downward-looking radiometers, the first term is clearly relevant only over ocean and strongest for horizontal polarization with very small optical thickness; the second term typically increases with the basal reflectivities and thus, generally, is bigger for greater optical thickness. Thus, the overall effect on T_Bs generally weakens with increasing optical thickness for the same $\Delta\tau$. On the other hand, if $\Delta\tau$ is assumed proportional to τ the maximum effect is found for optical thickness around 0.4. Therefore, in the cold front simulation the effect is expected to be greater than in the squall-line simulation, and this should generally be true for systems with the same basal reflectivity but with lower freezing levels. Moreover, the maximum variation in T_B is expected to correspond to an optical thickness equal to 0.3–0.5, that is, heavy precipitation at 10 GHz or low rain rates at 37 GHz.

c. Examples of modifications of T_Bs

Radiative transfer computations have been performed by using the Eddington approximation (Kummerow 1993). The T_Bs at a TMI viewing angle (53°) for the original CRM simulations have been computed and compared with the ones obtained with the melting layer model. The inclusion of melting can have a very strong (up to 60 K for some pixels very close to the convective raining cells) impact upon T_B, but generally it ranges between 10 and 23 K (a result shown in Fig. 8). The ΔT_B pattern closely follows the optical thickness excess so that the highest $\Delta\tau$ corresponds to the highest T_B increase. This means that the increase of absorption/emission because of the presence of mixed-phase particles [factor II in Eq. (19)] remains the leading factor in these simulations. At 37 GHz the T_Bs are much more correlated to the precipitating ice, which contributes substantially to the total optical thickness at this frequency. The enhancement due to melting is now strongly reduced (upper values around 30 K) and is no longer well correlated to the excess of optical thickness. In particular, for the pixels that have T_Bs close to the freezing level temperature, the effect must approach zero because factor I in Eq. (19) is very small.

In the squall-line simulation, as already predicted in section 4b, the introduction of mixed-phase hydrometeors has a substantially lower effect. Finally, a more modest increase of upwelling radiances is observed at 85.5 GHz for both simulations (a maximum radiance increase of 15 K is produced).

Table 3 summarizes the effect of including a melting layer upon TMI-footprint-averaged T_B for various parameterizations in different ground rainfall rate intervals for the cold front simulation. The profiler analysis by bracketing between models MG3 and FS2 improves the initial uncertainty between models ML96 and MG2 by an order of magnitude. While at 10.65 GHz the increase in the T_B intensifies with the rain rate and changes by as much as ~15–20 K according to our best matching models, at 19.35 GHz the maximum effect is found around 3–5 mm h^{-1} (~15 K), at 37 GHz the maximum effect is around 1 mm h^{-1} (~10 K), and at 85.5 GHz the effect is always lower than 3 K, almost insensitive to the electromagnetic model. Note that these estimates are valid for the cold front case, representing a system with a low freezing level, so that we believe they can be considered extreme variations.

Finally, an important consideration is that the uncertainty coming from the snow density is comparable to that coming from the knowledge of the correct electromagnetic model once the profiler discrimination has been carried out. For the same final raindrop population, high-density snow particles tend to have a smaller increase in T_B than fluffy ones, as already noticed by Bauer et al. (2000). Therefore, this parameter needs to be investigated for further improvements in the brightband impact on T_Bs.

5. Validation and planning for future measurements

The T_B modifications obtained for the CRMs, even when averaged over the large TMI footprints (e.g., see the results by Olson et al. (2001a,b)], can have a significant effect on the retrieved rainfall rates. Estimates of the biases have been given by Bauer et al. (1999), but they are largely dependent on the retrieval algorithm and on the various parameterizations used. These and our findings suggest that it is necessary to partially step back from the retrieval algorithm approach and focus on the real physical processes characterizing the melting layer (e.g., by using dedicated CRM simulations with spectral models, an explicit melting particle class, fine vertical resolution, and treatment of particle–particle in-

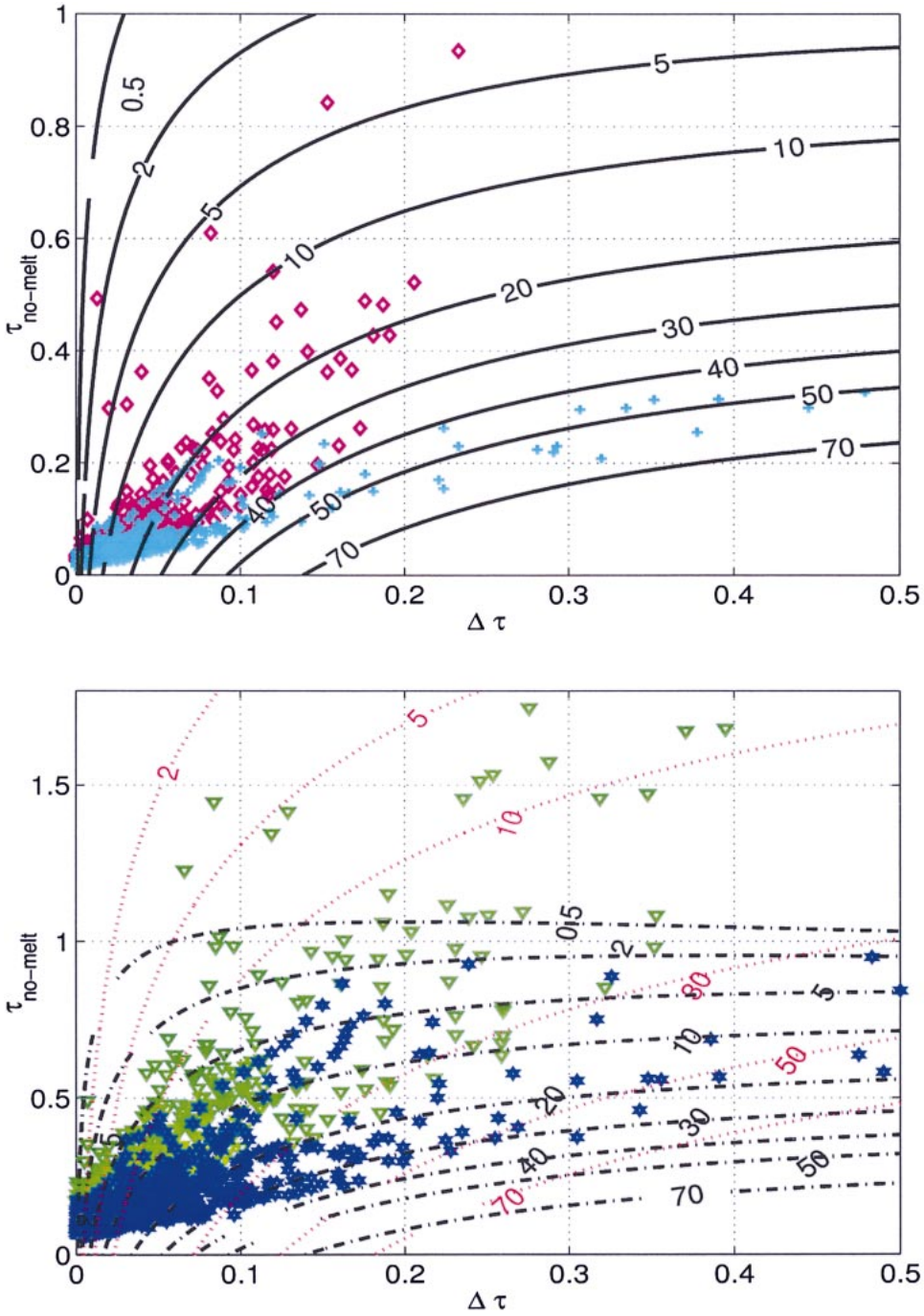

FIG. 8. Contour levels of the increase in T_B (horizontal polarization) over ocean as a function of the excess of optical thickness $\Delta\tau$ and of $\tau_{\text{no-melt}}$, the total optical thickness without the surplus due to melting. The computation is based on a very simple pure absorptive radiative transfer model with the average optical properties of the cold front (continuous lines) and the squall line (dash–dotted lines). Dotted lines are contour levels of ΔT_B for a ground-based nadir upward-looking radiometer. Also shown are some sample points computed from the cold front (crosses and pentagrams) and the squall line (diamonds and triangles) simulation at (top) 10.65 and (bottom) 19 GHz, respectively. Excess optical thickness $\Delta\tau$ has been computed with MG3 model 5.

TABLE 3. Increase in the T_Bs (K) due to the introduction of the melting layer at the TMI footprint for the cold front. For each electromagnetic model the first and the second lines have the lowest and the highest increases due to density model variation.

Frequency (GHz)	Electromagnetic model	Range of rainfall rates (mm h^{-1})				
		0.5–2.5	2.5–5	5–7.5	7.5–10	10–15
10.65	ML96	2.2 ± 1.6//1	3.4 ± 2.2//1	3.2 ± 1.4//1	3.7 ± 1.7//1	6.5 ± 2.3//1
		3.3 ± 2.4//6	4.7 ± 3.2//6	4.3 ± 1.9//6	5.0 ± 2.1//6	8.2 ± 2.9//6
	MG2	10.5 ± 7.9//2	15.1 ± 10.5//2	13.4 ± 6.1//2	15.7 ± 6.6//2	24.4 ± 8.1//2
		21.7 ± 16.2//6	29.1 ± 20//6	25.3 ± 11.7//6	28.9 ± 11//6	39.1 ± 12//6
	MG3	4.4 ± 3.3//1	6.6 ± 4.5//1	6.1 ± 2.7//1	7.1 ± 3.1//1	12 ± 4.2//1
		6.2 ± 4.6//6	8.8 ± 6.0//6	7.9 ± 3.5//6	9.1 ± 3.9//6	14.6 ± 5.0//6
	FS2	5.6 ± 4.3//1	8.4 ± 7.6//2	7.6 ± 3.4//2	8.9 ± 3.9//2	14.6 ± 5.1//2
		9.6 ± 7.2//6	13.5 ± 12.0//6	12.0 ± 5.4//6	13.9 ± 5.7//6	21.5 ± 7.3//6
37	ML96	4.8 ± 3.1//1	4.2 ± 2.5//2	2.5 ± 2.5//2	1.9 ± 1.8//2	1.6 ± 1.3//2
		5.8 ± 3.6//6	5.8 ± 3.4//6	4.7 ± 3.9//6	3.3 ± 3.3//6	3.2 ± 2.8//6
	MG2	10.9 ± 6.7//1	9.5 ± 5.4//2	6.3 ± 5.0//2	4.3 ± 4.0//2	3.7 ± 2.7//2
		17.2 ± 10.1//6	14 ± 7.6//6	9.5 ± 7.1//6	6.6 ± 6.1//6	5.8 ± 4.2//6
	MG3	7.0 ± 4.3//1	6.3 ± 3.7//1	6.3 ± 3.7//2	2.9 ± 2.8//2	2.5 ± 2.0//2
		8.2 ± 5.0//6	7.8 ± 4.5//6	7.8 ± 4.5//6	4.2 ± 4.1//6	4.0 ± 3.3//6
	FS2	7.8 ± 4.9//1	6.9 ± 4.0//2	4.7 ± 3.8//6	3.2 ± 3.0//2	2.8 ± 2.1//2
		10.5 ± 6.4//6	9.6 ± 5.4//6	7.0 ± 5.5//6	4.9 ± 4.7//6	4.5 ± 3.6//6

teractions, and by validating them against in situ measurements). This will become even more important for future algorithms that need to deal not only with a bright band but also with an uncertainty estimate for the bright-band extinction. To achieve this goal, uncertainties about microphysics and electromagnetic modeling have to be quantified.

From a physical modeling perspective, a better parameterization and validation of the fall speed and ventilation coefficient of melting particles is strongly recommended. In this context, tunnel measurements, similar to the ones performed by Mitra et al. (1990), may be useful to better understand how the distance to complete melting depends on the initial ice density. Field measurements of the dielectric constant coupled with detailed microphysical characterizations such as those performed by Prodi et al. (1996), with a scatterometer or with microwave attenuation links, can give important hints.

The most valuable measurement, however, would be a direct evaluation of the excess of optical thickness in the melting layer with a precision that allows discrimination of different parameterizations. It is possible to fly upward-looking multichannel radiometers on a pair of aircraft right above and below the melting layer, or to use a multifrequency radar flying just above the melting layer, to provide direct measurements of the extinction in the brightband region. Such schemes, however, are expensive and may not collect enough statistics.

We therefore explore ground-based possibilities. One such possibility is to compute the difference between the total optical thickness and the optical thickness due to hydrometeors outside the melting layer. While a ground-based multiwavelength radiometer can be used to obtain the total optical depth, a set of synergetic instruments must be set up to characterize the hydrometeor profiles outside the brightband region. A low-frequency profiler is particularly suited to determine the size distributions of the rain below the bright band and to get reflectivity and Doppler velocity profiles in a Rayleigh region; a cloud radar (35 or 94 GHz) seems appropriate to retrieve the structure of the clouds above the melting level and the cloud water, which may contribute to the total optical path but must be discriminated from the brightband optical excess. All measurements should preferably be accompanied by precise soundings in order to establish the humidity and temperature profiles.

In the ground-based configuration, the downwelling radiances should increase by approximately $\Delta T_B = \langle T_{\text{atm}} \rangle \exp(-\tau_{\text{no-melt}}) [1 - \exp(-\Delta\tau)]$. The contour lines of this quantity, drawn as dashed lines in Fig. 8, show a greater $\Delta T_B/\Delta\tau$ ratio for the same $\tau_{\text{no-melt}}$ (except for very thin layers).

From this experimental arrangement it seems possible to estimate the optical thickness excesses as a function of quantities like the basal reflectivities, the width of

the bright band, the background conditions, and the variation of mass fluxes from the freezing level to the basal level. The construction of this dataset should allow an estimate of the error in $\Delta\tau$ (and successively in the rain rates) and, finally, a better selection of the best-fitting microphysical and electromagnetic models. Other issues, like the climatological and spatial variability of the bright band on the footprint of typical spaceborne radiometers or the role played by graupel and snow in strengthening the extinction signal, have to be addressed also.

6. Summary and conclusions

This study focused on the variations in the extinction profiles and the optical thickness produced by the introduction of mixed-phase hydrometeors. A very simple methodology to reconstruct the vertical profile of scattering properties inside the melting layer has been developed by starting from the basal raindrop size distributions and going upward to the freezing level. The underlying reason to proceed in this way is based on the necessity to start from information that is relatively easy to derive from experimental measurements with current sensors. The methodology, applied to the profiler data acquired during the TRMM KWAJEX field campaign, allows us to reduce the uncertainties that come from different parameterizations of the microphysical processes and of the effective dielectric constants. The parameterization of Szyrmer [Eq. (8)] for the ventilation coefficient appears to be the most appropriate to fit the reflectivity and the Doppler velocity profiles compatibly with the average background conditions of the measurement site. The Mitra parameterization for oblate spheroids [Eq. (7)] gives the worst fit to the data because it tends to underestimate the distance for complete melting. However, these conclusions require a better understanding of the average background conditions inside the bright band. The brightband peak appears to be best represented (in the average sense) by using MG3 (almost equivalent to FS1) and FS2 dielectric constant models; ML96 generally underestimates the strength of the peak. While it is difficult to make specific inferences for particular parameterizations, most other schemes seem to forecast reflectivity profiles that are too far from the real data to be realistic in an average sense.

By using the one-dimensional melting model output from CRM simulations, the optical thickness excess has been computed as a function of the basal reflectivities for stratiform pixels. Results show that although there is high variability introduced by the physics of the CRM, the uncertainty due to the electromagnetic parameterization can probably be further refined by performing targeted measurements. Using the best matching model, the simulation of brightness temperatures for a mid-Atlantic cold front has given maximum radiance increases (up to 60 K for 10.35 GHz at the CRM resolution) even higher than those found by former investigators. At TMI resolution the maximum radiance increases are found at high rainfall rates at 10.35 GHz and at low rainfall rates at 37 GHz (Table 3 summarizes these results), which qualitatively agrees with our preliminary analysis with TMI-PR data, shown in Fig. 1. In the cold front simulation, the brightband effect is certainly enhanced by the fact that this CRM simulation has a very low freezing level, which underscores the importance of the melting layer in midlatitude scenarios. Finally, it seems that more precise conclusions will be possible only after more precise and detailed measurements of the extinction profiles inside the bright bands are made.

Acknowledgments. This research was supported by the National Aeronautics and Space Administration under Contract NAG5-11189 and by EURAINSAT, a shared-cost project (Contract EVG1-2000-00030) cofunded by the Research DG of the European Commission within the RTD activities of a generic nature of the Energy, Environment and Sustainable Development subprogram (Fifth Framework Programme). The authors also wish to thank W. K. Tao from NASA GSFC as well as Grant Petty and Christine Chiu for the model simulations.

REFERENCES

Atlas, D., R. C. Srivastava, and R. S. Sekhon, 1973: Doppler radar characteristics of precipitation at vertical incidence. *Rev. Geophys. Space Phys.*, **11,** 1–35.

Barthazy, E., W. Heinrich, and A. Waldvogel, 1998: Size distribution of hydrometeors through the melting layer. *Atmos. Res.*, **47–48,** 193–208.

Bauer, P., 2001: Including a melting layer in microwave radiative transfer simulation for clouds. *Atmos. Res.*, **57,** 9–30.

——, J. P. V. Poiares Baptista, and M. de Iulis, 1999: The effect of the melting layer on the microwave emission of clouds over the ocean. *J. Atmos. Sci.*, **56,** 852–867.

——, A. Khain, A. Pokrovsky, R. Meneghini, C. Kummerow, F. Marzano, and J. P. V. Poiares Baptista, 2000: Combined cloud–microwave radiative transfer modeling of stratiform rainfall. *J. Atmos. Sci.*, **57,** 1082–1104.

Carter, D. A., K. S. Gage, W. L. Ecklund, W. M. Angevine, P. E. Johnston, A. C. Riddle, J. Wilson, and C. R. Williams, 1995: Developments in lower tropospheric wind profiling at the NOAA Aeronomy Laboratory. *Radio Sci.*, **30,** 977–1001.

Chiu, J.-Y., and G. W. Petty, 2001: Comparisons of observed and simulated microwave images of extratropical cyclones. Preprints, *11th Conf. on Satellite Meteorology and Oceanography,* Madison, WI, Amer. Meteor. Soc., 524–527.

Fabry, F., and I. Zawadzki, 1995: Long-term radar observations of the melting layer of precipitation and their interpretation. *J. Atmos. Sci.*, **52,** 838–851.

——, and K. Szyrmer, 1999: Modeling of the melting layer. Part II: Electromagnetic. *J. Atmos. Sci.*, **56,** 3593–3600.

Heymsfield, A. J., A. Bansemer, P. R. Field, S. L. Durden, J. Stith, J. E. Dye, W. Hall, and T. Grainger, 2002: Observations and parameterizations of particle size distributions in deep tropical cirrus and stratiform precipitating clouds: Results from in situ observations in TRMM field campaigns. *J. Atmos. Sci.*, **59,** 3457–3491.

Iguchi, T., T. Kozu, R. Meneghini, J. Awaka, and K. Okamoto, 2000:

Rain-profiling algorithm for the TRMM precipitation radar. *J. Appl. Meteor.*, **39,** 2038–2052.

Klaassen, W., 1988: Radar observation and simulation of the melting layer of precipitation. *J. Atmos. Sci.*, **45,** 3741–3753.

Kummerow, C., 1993: On the accuracy of the Eddington approximation for radiative transfer in the microwave frequencies. *J. Geophys. Res.*, **98,** 2757–2765.

Locatelli, J. D., and P. V. Hobbs, 1974: Fall speeds and masses of solid precipitation particles. *J. Geophys. Res.*, **79,** 2185–2197.

Magano, C., and T. Nakamura, 1965: Aerodynamic studies of falling snowflakes. *J. Meteor. Soc. Japan*, **43,** 139–147.

Meneghini, R., and L. Liao, 1996: Comparisons of cross sections for melting hydrometeors as derived from dielectric mixing formulas and a numerical method. *J. Appl. Meteor.*, **35,** 1658–1670.

——, and ——, 2000: Effective dielectric constants of mixed-phase hydrometeors. *J. Atmos. Oceanic Technol.*, **17,** 628–640.

Mitchell, D. L., R. Zhang, and R. L. Pitter, 1990: Mass-dimensional relationships for ice particles and the influence of riming on snowfall rates. *J. Appl. Meteor.*, **29,** 153–163.

Mitra, S. K., O. Vohl, M. Ahr, and H. R. Pruppacher, 1990: A wind tunnel and theoretical study of the melting behavior of atmospheric ice particles. IV: Experiment and theory for snow flakes. *J. Atmos. Sci.*, **47,** 584–591.

Olson, W. S., P. Bauer, C. D. Kummerow, Y. Hong, and W. Tao, 2001a: A melting-layer model for passive/active microwave remote sensing applications. Part II: Simulation of TRMM observations. *J. Appl. Meteor.*, **40,** 1164–1179.

——, ——, N. F. Viltard, D. E. Johnson, W. K. Tao, R. Meneghini, and L. Liao, 2001b: A melting-layer model for passive/active microwave remote sensing applications. Part I: Model formulation and comparison with observations. *J. Appl. Meteor.*, **40,** 1145–1163.

Passarelli, R. E., and R. C. Srivastava, 1980: A new aspect of the vertical incidence Doppler radar spectrum of ice particle fallspeeds. *J. Appl. Meteor.*, **19,** 1318–1322.

Prodi, F., A. Moretti, and O. Sturniolo, 1996: Backscattering gain measurements of spherical ice hydrometeors at 35.8 GHz and comparison to numerical computation. *J. Atmos. Oceanic Technol.*, **13,** 407–418.

Pruppacher, H. R., and J. D. Klett, 1997: *Microphysics of Clouds and Precipitation.* Kluwer Academic, 954 pp.

Schaller, R. C., I. D. Cohen, A. A. Barnes, and L. C. Gibbons, 1982: A survey of melting layer research. AFGL Rep. TR-82-0007, 102 pp. [Available from Air Force Geophysical Laboratories, Hanscom Air Force Base, MA 01731.]

Szyrmer, K., and I. Zawadzki, 1999: Modeling of the melting layer. Part I: Dynamics and microphysics. *J. Atmos. Sci.*, **56,** 3573–3592.

Tao, W. K., and J. Simpson, 1993: Goddard cumulus ensemble model. Part I: Model description. *Terr. Atmos. Oceanic Sci.*, **4,** 35–72.

Williams, C., 2002: Simultaneous ambient air motion and raindrop size distributions retrieved from UHF vertical incident profiler observations. *Radio Sci.*, **37** (2), 1024, doi:10.1029/2000RS002603.

Yokoyama, T., and H. Tanaka, 1984: Microphysical processes of melting snowflakes detected by two-wavelength radar. Part I. Principle of measurement based on model calculation. *J. Meteor. Soc. Japan*, **62,** 650–666.